ELSEVIER

A second-order boundary-fitted projection method for free-surface flow computations

B. Yang [a], A. Prosperetti [a,b,*]

[a] *Department of Mechanical Engineering, The Johns Hopkins University, 223 Latrobe Hall, Charles St. at 34th St., Baltimore, MD 21218, USA*
[b] *Faculty of Applied Science and Burgerscentrum, University of Twente, AE 7500 Enschede, The Netherlands*

Abstract

This paper describes a new approach to the high-fidelity simulation of axisymmetric free-surface flows. A boundary-fitted grid is coupled with a new projection method for the solution of the Navier–Stokes equations with second-order accuracy in space and time. Two variants of this new method are developed by adapting two existing algorithms, suitable for prescribed velocity boundary conditions, to the case of prescribed normal and tangential stresses at the free boundary. A normal-mode analysis for a fixed-boundary problem confirms the second-order accuracy of the algorithms. The approach is validated by comparison with a Rayleigh–Plesset solution for an oscillating spherical bubble, with an analysis of shape oscillations, and with existing results for the buoyant rise of a deforming bubble for Reynolds numbers up to 200 and Weber numbers up to 12. In addition to the simulation of axisymmetric free-surface flows of intrinsic interest, the present approach is suitable for the validation of genuinely three-dimensional calculations.
© 2005 Elsevier Inc. All rights reserved.

Keywords: Free-surface flows; Boundary-fitted grids; Projection method

1. Introduction

The development of computational methods for free-surface fluid flows is a very active research area. Several approaches have been formulated and a considerable effort is being expended in their extension and improvement. The use of a fixed finite-difference grid over which the interface moves is particularly attractive for reasons of efficiency and flexibility and a large fraction of the contemporary work in this area makes use of this approach. Among the many approaches developed one may mention front tracking (see e.g. [5,1–4,6–10]), the volume of fluid method (see e.g. [11–16]), the level set method (see e.g. [17–23]), the ghost fluid method (see e.g. [24–26]), the immersed boundary method (see e.g. [27–29]), sharp interface methods (see e.g. [30–32,26,33]) and others [34,35].

---

[*] Corresponding author. Tel.: +1 410 5168534; fax: +1 410 5167254.
  E-mail address: prosperetti@jhu.edu (A. Prosperetti).

Irrespective of the approach followed, validation remains a crucial issue in the development of complex computational tools. Analytical solutions are often limited to such simple situations that it may not be possible to put to a stringent test the full algorithm of the code. Comparison with the results given by other codes becomes therefore one of the primary validation tools, which justifies the development of high-fidelity simulation methods. One such method relies on boundary-fitted coordinates. The type of problems that lend themselves to this approach is somewhat restricted in two-dimensional or axisymmetric situations, and severely limited in three dimensions due to the difficulty of generating an orthogonal grid. However, even with restricted applicability, such methods are attractive due to their accuracy which can generate "numerically exact" solutions for complex problems.

The objective of the present paper is to describe a method based on orthogonal boundary-fitted coordinates suitable for the study of complex near-surface phenomena and code validation for axisymmetric problems. The method has second-order accuracy in both space and time. The grid generation algorithm, based on the well-known approach of [36,37], was described earlier [38–40] and is summarized in Section 5. Two versions of the second-order projection method for the solution of the Navier–Stokes equations suitable for the prescribed pressure, rather than velocity, boundary conditions that arise in free-surface flows are described. These methods derive from the work of [41] and are presented in Sections 2–4. Section 6 describes the complete algorithm which is tested and validated in Section 7.

The considerable success of the early projection (or fractional step) methods has prompted several extensions to second-order accuracy in time (see e.g. [42–45,41,46–49]). All of these papers consider problems in which the boundary velocity is prescribed, which leads to a Neumann condition for the pressure or pressure-like variable. The situation is different in free-surface flows where typically a pressure or pressure jump is prescribed on at least part of the boundary. Very few papers consider second-order methods for this case [14,26,50–52]. In some of these [50,51,26], the free-surface boundary condition is incorporated directly into the discretization of the Poisson equation, so that the interface is not treated as a boundary for the pressure calculation. A disadvantage of this approach is that the pressure condition is approximated using pressure values near the interface, rather than at the interface itself. Ref. [52] uses the method of [53], where the boundary condition is introduced as a localized volume force and the free surface is diffused over a few grid cells, which may not be desirable for certain applications. Ref. [14] is only concerned with surface convection by a prescribed velocity field and the subsequent reconstruction.

The seemingly minor modification of imposing pressure conditions at the boundary has important consequences for the projection method because, if the Poisson equation is solved with Dirichlet conditions, the incompressibility constraint is not automatically satisfied at the boundary [54,55]. This point is very important because, as shown in [41], the treatment of boundary conditions is crucial to achieve second-order accuracy for the pressure field and, therefore, this issue did not arise in the many first-order algorithms available in the literature (see e.g. [56–59,24,9] and many others).

2. Two second-order projection methods for free-surface flows

The differential form of the problem we consider in this paper consists of the Navier–Stokes equations for an incompressible liquid

$$\nabla \cdot \mathbf{u} = 0, \tag{1}$$

$$\frac{\partial \mathbf{u}}{\partial t} + \mathbf{u} \cdot \nabla \mathbf{u} = -\frac{1}{\rho} \nabla p + v \nabla^2 \mathbf{u} + \mathbf{g} \tag{2}$$

in which $\mathbf{u}$ is the velocity, p the pressure, ρ the density, v the kinematic viscosity, and $\mathbf{g}$ the body force, subject to conditions at a free surface separating the liquid from a gas having negligible inertia and viscosity. With this assumption, the effect of the gas reduces to imposing a pressure p_g – either known or calculated by other means – and the vanishing of the tangential stresses:

$$p = p_g - \sigma C + \mu \mathbf{n} \cdot (\nabla \mathbf{u} + \nabla \mathbf{u}^T) \cdot \mathbf{n}, \tag{3}$$

$$\mathbf{t} \cdot (\nabla \mathbf{u} + \nabla \mathbf{u}^T) \cdot \mathbf{n} = 0. \tag{4}$$

Here σ is the surface tension coefficient, C the surface curvature, $\mathbf{n}$ the unit normal directed into the gas, $\mathbf{t}$ a unit vector in the tangential direction, and the superscript T denotes the transpose. The interface position is updated by integrating

$$\frac{d\mathbf{x}}{dt} = \mathbf{u}(\mathbf{x}, t), \tag{5}$$

where $\mathbf{x}$ is the generic interface point.

We consider two variants of the projection method of [41], both accurate to second order in space and time, and both originally developed for prescribed-velocity boundary conditions. Both variants use an intermediate velocity $\mathbf{u}^*$ and a pressure-like variable ϕ in terms of which the end-of-time-step velocity $\mathbf{u}^{n+1}$ is given by

$$\mathbf{u}^{n+1} = \mathbf{u}^* - \frac{\Delta t}{\rho} \nabla_h \phi^{n+1} \tag{6}$$

in which ∇_h is a second-order-accurate discrete approximation to the gradient operator; $\mathbf{u}^*$ and ϕ are related to each other by the Poisson equation

$$\Delta t \nabla_h^2 \phi^{n+1} = \rho \nabla_h \cdot \mathbf{u}^*. \tag{7}$$

The difference between the two variants lies in the definition of u^* and the relation between p and ϕ. In the first method, ϕ is essentially the increment necessary to update the pressure from time level $n - 1/2$ to time level $n + 1/2$; we refer to this method as the pressure-increment method. For the second method – referred to as pressure-free method – ϕ essentially represents the new pressure field. We carry both methods at the same time by writing

$$p^{n+1/2} = \beta p^{n-1/2} + \phi^{n+1} - \frac{\nu \Delta t}{2} \nabla_h^2 \phi^{n+1}, \tag{8}$$

where

$$\beta = \begin{cases} 1 & \text{pressure-increment method,} \\ 0 & \text{pressure-free method} \end{cases} \tag{9}$$

and $\mathbf{u}^*$ is the solution of

$$\frac{\mathbf{u}^* - \mathbf{u}^n}{\Delta t} + \frac{\beta}{\rho} \nabla_h p^{n-1/2} = -[(\mathbf{u} \cdot \nabla_h)\mathbf{u}]^{n+1/2} + \frac{\nu}{2} \nabla_h^2 (\mathbf{u}^n + \mathbf{u}^*) + \mathbf{g} \tag{10}$$

in which $[(\mathbf{u} \cdot \nabla_h)\mathbf{u}]^{n+1/2}$ is a second-order-accurate discretization of the convective term.

In the *original formulation* of [41] developed for a prescribed velocity $\mathbf{u}_b$ at the boundary, the pressure Poisson equation (7) is solved subject to the Neumann condition

$$(\mathbf{n} \cdot \nabla_h \phi^{n+1})|_{\partial\Omega} = 0, \tag{11}$$

while the boundary conditions for the Helmholtz equation (10) for $\mathbf{u}^*$ are

$$\mathbf{n} \cdot \mathbf{u}^*|_{\partial\Omega} = \mathbf{n} \cdot \mathbf{u}_b^{n+1}, \tag{12}$$

$$\mathbf{t} \cdot \mathbf{u}^*|_{\partial\Omega} = \mathbf{t} \cdot \mathbf{u}_b^{n+1} + (1 - \beta)\frac{\Delta t}{\rho} \nabla_h \phi^n|_{\partial\Omega}. \tag{13}$$

In the *present formulation*, in which it is the pressure on (part of) the boundary to be prescribed rather than the velocity, the boundary conditions need to be modified. According to the analysis of [41], an essential feature necessary to ensure second-order time accuracy for the pressure all the way up to the boundary is the absence of boundary layers in the intermediate velocity $\mathbf{u}^*$. A consideration of this result and of the relation (8) between ϕ and p suggests then to impose

$$\nabla_h^2 \phi^{n+1} = 0 \tag{14}$$

on the free surface, as a consequence of which, from (7),

$$\nabla_h \cdot \mathbf{u}^*|_{\partial\Omega} = 0 \tag{15}$$

on the free surface. As shown in Sections 4 and 5, this equation can be used to obtain an estimate of $\mathbf{u}^* \cdot \mathbf{n}$ on the free surface thus replacing (12). Since $\mathbf{u}$ and p are expected to be smooth near the interface, (6) and (8) suggest that, with this choice, $\mathbf{u}^*$ should also be smooth. From (8), the boundary condition for ϕ is then

$$\phi^{n+1} = p^{n+1/2} - \beta p^{n-1/2}$$
$$= p_g^{n+1/2} - \beta p^{n-1/2} - \sigma C^{n+1/2} + \mu \mathbf{n}^{n+1/2} \cdot [\nabla_h \mathbf{u}^{n+1/2} + (\nabla_h \mathbf{u}^{n+1/2})^{\mathrm{T}}] \cdot \mathbf{n}^{n+1/2} \tag{16}$$

which replaces (11) for the solution of the Poisson equation. Since this relation applies on the free surface, the term $\nabla_h^2 \phi$ appearing in the pressure relation (8) is absent due to (14). The normal mode analysis presented in the next section illustrates the role of the condition (15) in securing second-order time accuracy. A finite-difference approximation to the tangential stress condition

$$\mathbf{t}^{n+1} \cdot [\nabla_h \mathbf{u}^* + (\nabla_h \mathbf{u}^*)^{\mathrm{T}}] \cdot \mathbf{n}^{n+1} = \frac{\Delta t}{\rho} \mathbf{t}^{n+1} \cdot [\nabla_h \nabla_h \phi^{n+1} + (\nabla_h \nabla_h \phi^{n+1})^{\mathrm{T}}] \cdot \mathbf{n}^{n+1} = 0 \tag{17}$$

is a suitable replacement for (13), while all other elements of the methods remain unchanged.

In summary, the present method consists of calculating $\mathbf{u}^*$ from (10) subject to the conditions (15) and (17), ϕ from (7) subject to (16), and updating the interface position from (5).

The boundary conditions for the calculation of the velocity and pressure fields need to be imposed on the updated interface. In order to avoid the need for an iterative process with a new grid generated at each iteration, we choose the leap-frog scheme to update the free surface position:

$$\mathbf{x}^{n+1} = \mathbf{x}^{n-1} + 2\Delta t \mathbf{u}^n. \tag{18}$$

We also tried a second- and third-order Adams–Bashforth scheme with negligible differences. Both methods are explicit and, therefore, they imply a limitation on the time step, which must be sufficiently smaller than the period of the shortest capillary waves, of the order of $\sqrt{\rho h^3/\sigma}$, in which h is the node spacing along the free surface. In the examples that follow this limitation is less stringent than that deriving from the Courant condition.

For the calculation of $[(\mathbf{u} \cdot \nabla_h)\mathbf{u}]^{n+1/2}$, we use the second-order Adams–Bahsforth time discretization. As this scheme is not self-starting, the first step is executed with a trapezoidal-rule time discretization with the resulting non-linear equations solved by iteration.

3. Normal mode analysis

In order to demonstrate that the two methods as modified above remain second-order in time, it is useful to have recourse to a standard normal-mode analysis [60,44,61]. We formulate a differential problem mimicking the original one in its mathematical structure. Then we consider its semi-discrete version according to the projection methods as modified before, solve it, and show that the difference with the exact solution is $O(\Delta t^2)$.

We linearize the Navier–Stokes momentum equation by replacing the non-linear term with a forcing $\mathbf{f}$ and set $\rho = 1$ for simplicity:

$$\frac{\partial \mathbf{u}}{\partial t} = -\nabla p + v\nabla^2 \mathbf{u} + \mathbf{f} \tag{19}$$

and solve this equation in the two-dimensional semi-infinite strip $\Omega = [0, \infty) \times [-\pi, \pi]$, subject to the incompressibility constraint (1), periodicity conditions at $y = \pm\pi$ and, at $x = 0$,

$$p(0, y, t) = p_g(y, t), \quad \frac{\partial u}{\partial y} + \frac{\partial v}{\partial x} = 0 \tag{20}$$

in which $p_g(y, t)$ is a prescribed function and $u = u_x$, $v = u_y$. The fields are required to vanish as $x \to \infty$.

The pressure Poisson equation generated by taking the divergence of the linearized momentum equation (19)

$$\nabla^2 p = \nabla \cdot \mathbf{f} \tag{21}$$

can be solved by expanding in a Fourier series in y, so that

$$(-\partial_x^2 + k^2)\hat{p} = -\left(\frac{\partial \hat{f}_x}{\partial x} + ik\hat{f}_y\right) \equiv -\tilde{f}, \tag{22}$$

where $k > 0$ is the wave number and the caret indicates the corresponding Fourier mode. The solution is

$$\hat{p} = \hat{p}_g e^{-kx} + \frac{1}{2k} \int_0^\infty e^{-k|x-\xi|} \tilde{f} \, d\xi - \frac{e^{-kx}}{2k} \int_0^\infty e^{-k\xi} \tilde{f} \, d\xi. \tag{23}$$

With this expression for $\hat{p}$, the Fourier modes $\hat{\mathbf{u}}$ of the velocity are readily found from (19):

$$(-\partial_x^2 + k^2 + s/v)\hat{\mathbf{u}} = -\frac{1}{v}\nabla\hat{p} + \frac{1}{v}\hat{\mathbf{f}}, \tag{24}$$

with s the Laplace variable conjugate to time.

The semi-discrete momentum equation corresponding to (10) is now:

$$\frac{\mathbf{u}^* - \mathbf{u}^n}{\Delta t} + \beta \nabla p^{n-1/2} = \frac{v}{2} \nabla^2 (\mathbf{u}^* + \mathbf{u}^n) + \mathbf{f}^{n+1/2}. \tag{25}$$

After eliminating $\mathbf{u}^*$ by means of the projection $\mathbf{u}^* = \mathbf{u}^{n+1} + \Delta t \nabla \phi^{n+1}$, we have

$$\frac{\mathbf{u}^{n+1} - \mathbf{u}^n}{\Delta t} + \nabla \phi^{n+1} + \beta \nabla p^{n-1/2} = \frac{v}{2} \nabla^2 (\mathbf{u}^{n+1} + \mathbf{u}^n) + \frac{v\Delta t}{2} \nabla^2 \nabla \phi^{n+1} + \mathbf{f}^{n+1/2}. \tag{26}$$

Furthermore, the formula (8) used to update the pressure gives

$$\hat{p} = \kappa^{1/2} \frac{v\Delta t}{2} \left(1 + \frac{\beta}{\kappa - 1}\right)(-\partial_x^2 + \gamma^2)\hat{\phi} \tag{27}$$

with which, after a Fourier expansion and Laplace transformation, Eq. (26) becomes

$$(-\partial_x^2 + \lambda^2)\hat{\mathbf{u}} = \frac{\kappa \Delta t}{\kappa + 1} \left(1 + \frac{\beta}{\kappa - 1}\right)(\partial_x^2 - \gamma^2)\nabla\hat{\phi} + \frac{2\kappa^{1/2}}{v(\kappa + 1)}\hat{\mathbf{f}} \tag{28}$$

in which β is defined in (9) and

$$\kappa = e^{s\Delta t}, \quad \lambda = \sqrt{k^2 + r/v}, \quad r = \frac{2(\kappa - 1)}{\Delta t(\kappa + 1)}, \quad \gamma = \sqrt{k^2 + \frac{2}{v\Delta t}}. \tag{29}$$

Upon taking the divergence of (28), one finds

$$(-\partial_x^2 + \gamma^2)(-\partial_x^2 + k^2)\hat{\phi} = -\left(1 - \frac{\beta}{\kappa}\right)\frac{2}{v\Delta t \kappa^{1/2}}\tilde{f}. \tag{30}$$

The boundary conditions $\nabla \cdot \mathbf{u}^* = 0$ and $p(0, y, t) = p_g(y, t)$ at $x = 0$ become

$$(\partial_x^2 - k^2)\hat{\phi} = 0, \quad \hat{\phi} = \frac{1}{\kappa^{1/2}}\left(1 - \frac{\beta}{\kappa}\right)\hat{p}_g \tag{31}$$

the solution of which is

$$\hat{\phi} = \frac{1}{2k\kappa^{1/2}}\left(1 - \frac{\beta}{\kappa}\right)\left[2k\hat{p}_g e^{-kx} + \int_0^\infty e^{-k|x-\xi|}\tilde{f} \, d\xi - e^{-kx}\int_0^\infty e^{-k\xi}\tilde{f} \, d\xi\right]$$
$$- \left(1 - \frac{\beta}{\kappa}\right)\frac{1}{2\gamma\kappa^{1/2}}\left[\int_0^\infty e^{-\gamma|x-\xi|}\tilde{f} \, d\xi - e^{-\gamma x}\int_0^\infty e^{-\gamma\xi}\tilde{f} \, d\xi\right]. \tag{32}$$

When this result is substituted into (27), the spurious modes proportional to $\exp\pm\gamma x$ are eliminated and one recovers the exact result (23) for the pressure. The momentum equation (28) becomes instead

$$(-\partial_x^2 + \lambda^2)\hat{\mathbf{u}} = -\frac{\alpha}{v}\nabla\hat{p} + \frac{\alpha}{v}\nabla\hat{\mathbf{f}}. \tag{33}$$

In comparing this equation with the exact one (24) derived earlier, we note that

$$\alpha \equiv \frac{2\kappa^{1/2}}{\kappa + 1} = 1 + \mathrm{O}(s^2\Delta t^2), \quad \lambda = \sqrt{k^2 + s/v} + \mathrm{O}(s^2\Delta t^2), \tag{34}$$

which show that the difference is of second order in time.

4. A preliminary numerical test

In order to confirm the error estimate given by the normal-mode analysis, we carry out a preliminary test for a simple two-dimensional case in which the exact solution of the problem (1)–(4) with $\rho = 1$ and $v = 1$ in the domain $0 \leqslant x, y \leqslant (1/2)\pi$ is given by

$$\begin{aligned}
u(x,y,t) &= -\cos x \sin y\,\mathrm{e}^{-2t}, \\
v(x,y,t) &= \sin x \cos y\,\mathrm{e}^{-2t}, \\
p(x,y,t) &= -\tfrac{1}{4}(\cos 2x + \cos 2y)\,\mathrm{e}^{-4t}.
\end{aligned} \tag{35}$$

For this solution, $\partial u/\partial y + \partial v/\partial x = 0$ and, therefore, the tangential stress vanishes at $y = 0$ and $y = (1/2)\pi$. In the numerical solution, on these two lines we impose the exact value of the pressure and zero tangential stress, while the exact velocity is prescribed at $x = 0$ and $x = (1/2)\pi$.

The computational domain is discretized by using the same step h in the two spatial directions and a constant time step of $\Delta t = (1/2)h$, so that the Courant number equals 1/2.

We adopt a standard staggered grid arrangement with the pressure and ϕ defined at cell centers and the velocity components at cell boundaries. The grid near the boundary $y = (1/2)\pi$ is sketched in Fig. 1, in which circles represent the p or ϕ points, squares the u points, and triangles the v points. For the Poisson equation, $\partial^2 p/\partial y^2$ at point (i, J) is approximated by the second-order-accurate one-sided formula involving $p_{i,J+1/2}$, and $p_{i,J}$, $p_{i,J-1}$. The condition $\nabla \cdot \mathbf{u}^* = 0$ at $(i, J + 1/2)$ is used to generate an equation for $v_{i,J+1/2}^*$ and imposed in the form

$$0 = (\nabla \cdot \mathbf{u}^*)_{i,J+1/2} = \tfrac{3}{2}(\nabla_h \cdot \mathbf{u}^*)_{i,J} - \tfrac{1}{2}(\nabla_h \cdot \mathbf{u}^*)_{i,J-1} + \mathrm{O}(h^2), \tag{36}$$

where the divergences in the right-hand side are approximated by the usual second-order formula.

Calculations are done with grids of 40×40, 80×80, 120×120 cells. Errors are calculated by comparison with the analytic solution at time $t = 0.196$ in both L_1 and L_∞ norms. Table 1 shows the errors for the pressure and the u- and v-components of the velocity for the pressure-free method; the numbers shown were normalized
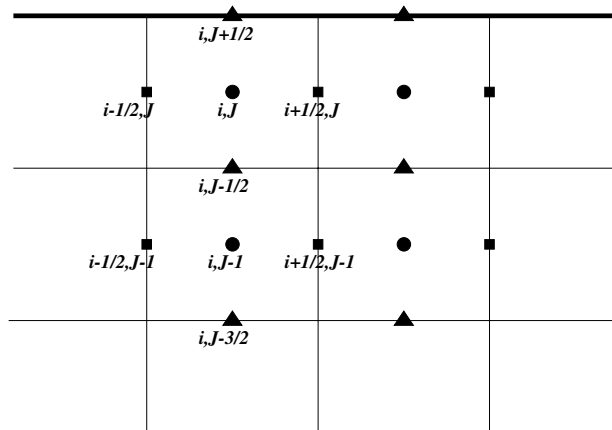

Fig. 1. Staggered grid near the free boundary.

Table 1
Normalized L_1- and L_∞-errors in the pressure and the velocity for the preliminary test of Section 4 with the pressure-free method for different discretizations with a fixed Courant number equal to 0.5

	40×40	80×80	120×120	Rate
Pressure				
L_1	4.35e − 4	1.14e − 4	5.20e − 5	1.93
L_∞	1.23e − 3	3.26e − 4	1.51e − 4	1.92
u-Component of velocity				
L_1	5.11e − 6	1.07e − 6	4.48e − 7	2.22
L_∞	1.29e − 5	2.75e − 6	1.19e − 6	2.18
v-Component of velocity				
L_1	1.82e − 5	3.85e − 6	1.43e − 6	2.31
L_∞	4.03e − 5	8.34e − 6	3.30e − 6	2.28

by $p_{max} = 1/4$ for the pressure. Table 2 shows the analogous results for the pressure-increment method. The convergence rates are computed using a linear fitting of the results for the three different grids and give results very close to 2 as expected. An example of the variation of the normalized maximum error in p with different mesh sizes for the pressure-increment method is shown in Fig. 2 on a logarithmic scale. The analogous plots for all quantities for both methods are very similar.

Table 2
Normalized L_1- and L_∞-errors in the pressure and the velocity for the preliminary test of Section 4 with the pressure-increment method for different discretizations with a fixed Courant number equal to 0.5

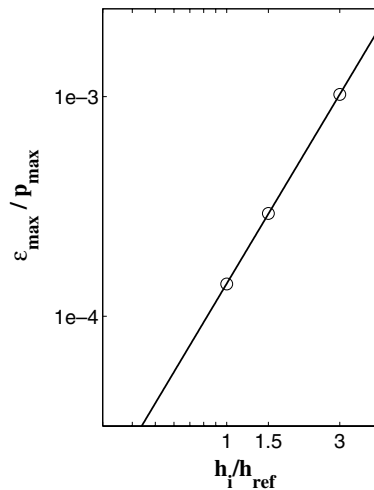|	40×40	80×80	120×120	Rate
Pressure				
L_1	3.19e − 4	8.27e − 5	4.22e − 5	1.85
L_∞	1.02e − 3	2.94e − 4	1.40e − 4	1.81
u-Component of velocity				
L_1	3.28e − 5	8.70e − 6	4.23e − 6	1.87
L_∞	7.44e − 5	1.92e − 5	9.62e − 6	1.87
v-Component of velocity				
L_1	1.07e − 4	2.87e − 5	1.18e − 5	2.00
L_∞	2.27e − 4	5.81e − 5	2.58e − 5	1.98

Fig. 2. Normalized maximum pressure error as a function of mesh refinement for the example of Section 4.

In general, for a second-order method, any measure ϵ of the error may be expected to have the form $\epsilon = A(\Delta t)^2 + Bh^2$, where A and B are related to derivatives of the quantities being calculated. Due to the Courant number stability limitations, the contribution of the time step is either comparable to, or smaller than, that of the spatial step so that the effect of Δt cannot be brought out simply by changing the time step. To circumvent this problem, we carry out N simulations with the same h and time steps $\Delta t_1, \Delta t_2, \ldots, \Delta t_N$ and define errors ϵ_k as the norm of the difference between the simulation with $\Delta t = \Delta t_k$ and that with the smallest time step, for which the error is dominated by the spatial discretization. By considering the ratios $\epsilon_k/\epsilon_{k+1}$, we can then test whether the exponent of Δt in the expression for the error is indeed 2. The results of this analysis, with a 40×40 grid and $\Delta t_1 = 0.6h$, $\Delta t_2 = 0.5h$, $\Delta t_3 = 0.4h$, and a smallest time step $\Delta t_4 = 0.04h$, are shown in Tables 3 and 4; these values were calculated at $t = 6h = 0.236$.

5. Boundary-fitted coordinates

For the solution of actual free-surface problems, we implement the algorithm described in the previous sections in conjunction with boundary-fitted coordinates generated according to the method of [36] as developed in [38]. The boundary-fitted coordinates (ξ, η) are generated by solving

$$\left[\frac{\partial}{\partial \xi} \left(f \frac{\partial}{\partial \xi} \right) + \frac{\partial}{\partial \eta} \left(\frac{1}{f} \frac{\partial}{\partial \eta} \right) \right] \binom{r}{x} = 0, \tag{37}$$

where (r, x) are cylindrical coordinates, $f = h_\eta/h_\xi$ is the distortion function defined in terms of the scale factors $h_\xi = (g_{\xi\xi})^{1/2}$ and $h_\eta = (g_{\eta\eta})^{1/2}$, with g the metric tensor. We take ξ tangential and η normal to the free surface, with $\eta = 0$ the outer boundary and $\eta = 1$ the free surface; for both coordinates $0 \leqslant \xi, \eta \leqslant 1$.

The continuity and momentum equations in (ξ, η) coordinates are (see e.g. [62])

Table 3
Normalized L_1- and L_∞-errors in the pressure and the velocity for the preliminary test of Section 4 with the pressure-free method for different time steps on a 40×40 grid

	Δt_1	Δt_2	Δt_3	Rate
Pressure				
L_1	$3.72e-4$	$2.50e-4$	$1.53e-4$	2.19
L_∞	$1.30e-3$	$8.72e-4$	$5.25e-4$	2.24
u-Component of velocity				
L_1	$1.36e-5$	$9.06e-6$	$5.45e-6$	2.26
L_∞	$4.03e-5$	$2.72e-5$	$1.68e-5$	2.15
v-Component of velocity				
L_1	$9.59e-5$	$6.77e-5$	$4.42e-5$	1.91
L_∞	$1.49e-4$	$1.04e-4$	$6.76e-5$	1.95

Table 4
Normalized L_1- and L_∞-errors in the pressure and the velocity for the preliminary test of Section 4 with the pressure-increment method for different time steps on a 40×40 grid

	Δt_1	Δt_2	Δt_3	Rate
Pressure				
L_1	$4.19e-4$	$2.95e-4$	$1.97e-4$	1.85
L_∞	$1.40e-3$	$9.60e-4$	$5.96e-4$	2.11
u-Component of velocity				
L_1	$1.43e-5$	$9.60e-6$	$5.82e-6$	2.22
L_∞	$4.30e-5$	$2.96e-5$	$1.88e-5$	2.04
v-Component of velocity				
L_1	$8.91e-5$	$6.24e-5$	$4.04e-5$	1.95
L_∞	$1.40e-4$	$9.70e-5$	$6.24e-5$	1.99

$$\frac{1}{h_\xi h_\eta r}\left[\frac{\partial}{\partial\xi}(h_\eta r u_\xi)+\frac{\partial}{\partial\eta}(h_\xi r u_\eta)\right]=0,\tag{38}$$

$$\frac{\partial u_\xi}{\partial t}+\frac{1}{h_\xi h_\eta r}\left[\frac{\partial}{\partial\xi}(h_\eta r u_\xi^2)+\frac{\partial}{\partial\eta}(h_\xi r u_\xi u_\eta)\right]$$
$$=-\frac{1}{\rho}\frac{1}{h_\xi}\frac{\partial p}{\partial\xi}+\frac{1}{h_\xi}\frac{\partial x}{\partial\xi}g+S_{\xi1}+S_{\xi2}+\frac{v}{h_\xi h_\eta r}\left[\frac{\partial}{\partial\xi}\left(\frac{h_\eta r}{h_\xi}\frac{\partial u_\xi}{\partial\xi}\right)+\frac{\partial}{\partial\eta}\left(\frac{h_\xi r}{h_\eta}\frac{\partial u_\xi}{\partial\eta}\right)\right],\tag{39}$$

$$\frac{\partial u_\eta}{\partial t}+\frac{1}{h_\xi h_\eta r}\left[\frac{\partial}{\partial\xi}(h_\eta r u_\xi u_\eta)+\frac{\partial}{\partial\eta}(h_\xi r u_\eta^2)\right]$$
$$=-\frac{1}{\rho}\frac{1}{h_\eta}\frac{\partial p}{\partial\eta}+\frac{1}{h_\eta}\frac{\partial x}{\partial\eta}g+S_{\eta1}+S_{\eta2}+\frac{v}{h_\xi h_\eta r}\left[\frac{\partial}{\partial\xi}\left(\frac{h_\eta r}{h_\xi}\frac{\partial u_\eta}{\partial\xi}\right)+\frac{\partial}{\partial\eta}\left(\frac{h_\xi r}{h_\eta}\frac{\partial u_\eta}{\partial\eta}\right)\right],\tag{40}$$

where (u_ξ, u_η) are velocity components in (ξ,η) directions and $S_{\xi1}$, $S_{\xi2}$ are given by

$$S_{\xi1}=-u_\eta\frac{h_\xi}{r_\xi}\frac{\partial}{\partial t}\left(\frac{x_\xi}{h_\xi}\right)+\frac{1}{J}\left(r_\eta\frac{\partial u_\xi}{\partial\xi}-r_\xi\frac{\partial u_\xi}{\partial\eta}\right)\frac{\partial x}{\partial t}+\frac{1}{J}\left(x_\xi\frac{\partial u_\xi}{\partial\eta}-x_\eta\frac{\partial u_\xi}{\partial\xi}\right)\frac{\partial r}{\partial t}$$
$$+\frac{\partial x}{\partial t}\left[\frac{u_\eta}{J}\left(\frac{r_\eta}{h_\eta}\frac{\partial h_\xi}{\partial\eta}+\frac{r_\xi}{h_\xi}\frac{\partial h_\eta}{\partial\xi}\right)\right]-\frac{\partial r}{\partial t}\left[\frac{u_\eta}{J}\left(\frac{x_\eta}{h_\eta}\frac{\partial h_\xi}{\partial\eta}+\frac{x_\xi}{h_\xi}\frac{\partial h_\eta}{\partial\xi}\right)\right],\tag{41}$$

$$S_{\xi2}=\frac{u_\eta^2}{J}\frac{\partial h_\eta}{\partial\xi}-\frac{u_\xi u_\eta}{J}\frac{\partial h_\xi}{\partial\eta}-\frac{v r_\xi}{r^2 h_\xi}\left(r_\xi\frac{u_\xi}{h_\xi}+r_\eta\frac{u_\eta}{h_\eta}\right)-\frac{v}{J^2}\left[u_\xi\left(\frac{\partial h_\xi}{\partial\eta}\right)^2+u_\xi\left(\frac{\partial h_\eta}{\partial\xi}\right)^2\right]$$
$$+\frac{v}{J}\left(\frac{\partial h_\xi}{\partial\eta}\frac{1}{h_\xi}\frac{\partial u_\eta}{\partial\xi}-\frac{\partial h_\eta}{\partial\xi}\frac{1}{h_\eta}\frac{\partial u_\eta}{\partial\eta}\right)+v\left[\frac{1}{h_\xi}\frac{\partial}{\partial\xi}\left(\frac{u_\eta}{J}\frac{\partial h_\xi}{\partial\eta}\right)-\frac{1}{h_\eta}\frac{\partial}{\partial\eta}\left(\frac{u_\eta}{J}\frac{\partial h_\eta}{\partial\xi}\right)\right],\tag{42}$$

where $J=h_\xi h_\eta$, $x_\xi=\partial x/\partial\xi$, $x_\eta=\partial x/\partial\eta$, $r_\xi=\partial r/\partial\xi$, $r_\eta=\partial r/\partial\eta$. $S_{\eta1}$ and $S_{\eta2}$ are similar with ξ and η interchanged.

The zero tangential stress condition and the normal stress condition on the free surface can be expressed as

$$\frac{h_\xi}{h_\eta}\frac{\partial}{\partial\eta}\left(\frac{u_\xi}{h_\xi}\right)+\frac{h_\eta}{h_\xi}\frac{\partial}{\partial\xi}\left(\frac{u_\eta}{h_\eta}\right)=0,\tag{43}$$

$$-p+2\mu\left(\frac{u_\xi}{h_\xi h_\eta}\frac{\partial h_\eta}{\partial\xi}+\frac{1}{h_\eta}\frac{\partial u_\eta}{\partial\eta}\right)=-p_g+\sigma C.\tag{44}$$

The curvature is calculated from the cubic spline fit of the free surface which is used in the grid generation process as explained in [38].

If η is the coordinate normal to the free-surface located in correspondence of $j=J+1/2$, the explicit form of the equation for u_η^* at the boundary generated from (36) is

$$u_{\eta_{i,J+1/2}}^*=\frac{1}{(h_\xi r)_{i,J+1/2}}\left\{\frac{1}{3}\frac{(h_\xi h_\eta r)_{i,J}}{(h_\xi h_\eta r)_{i,J-1}}\left[\frac{\Delta\eta}{\Delta\xi}(h_\eta r u_\xi^*)_{i+1/2,J-1}-\frac{\Delta\eta}{\Delta\xi}(h_\eta r u_\xi^*)_{i-1/2,J-1}+(h_\xi r u_\eta^*)_{i,J-1/2}-(h_\xi r u_\eta^*)_{i,J-3/2}\right]\right.$$
$$\left.-\frac{\Delta\eta}{\Delta\xi}(h_\eta r u_\xi^*)_{i+1/2,J}+\frac{\Delta\eta}{\Delta\xi}(h_\eta r u_\xi^*)_{i-1/2,J}+(h_\xi r u_\eta^*)_{i,J-1/2}\right\}.\tag{45}$$

6. Numerical implementation

All the derivatives appearing in the previous equations are calculated on a staggered grid by standard second-order-accurate formulae in the computational coordinates.

The computational sequence is the same for both projection methods described in Section 2. Velocity boundaries are treated as in the original projection method. On free boundaries, at the generic time level t^n, the steps are the following:

(1) Advance the free surface position to the next time level $\mathbf{x}^{n+1}$ by using (18).
(2) Generate an orthogonal boundary-fitted grid from this updated free-surface configuration as explained in the previous section.
(3) Calculate (if necessary) the new pressure on the gas side of the interface to be used as boundary condition for the liquid pressure.
(4) Use the projection algorithm to calculate new estimates of $\mathbf{u}^{n+1}$ and $p^{n+1/2}$, enforcing the normal and tangential stress conditions on the free surface.

Execution of the last step requires iteration as: (i) the two components of $\mathbf{u}^*$ are connected by the condition of zero divergence on the boundary and (ii) the stress boundary conditions involve $\mathbf{u}$ (and, therefore, ϕ^{n+1}) rather than $\mathbf{u}^*$. We therefore proceed as follows:

(a) A provisional estimate of $\mathbf{u}^{n+1}$ is calculated from (6) using the most recent values of $\mathbf{u}^*$ and ϕ^{n+1}; for the first step the values at time t^n are used.
(b) With this estimate, the value of the normal component u_η^* of the intermediate velocity at the boundary is updated from (45) in which the previous $\mathbf{u}^*$ is used in the right-hand side.
(c) The value of the tangential component u_ξ^* of the intermediate velocity at the boundary is updated from the tangential stress condition (43) after substitution of (6) using the current estimates of the velocity $\mathbf{u}^{n+1}$ and ϕ^{n+1}.
(d) A new pressure at the boundary is calculated from the normal stress condition (44).
(e) One ADI sweep is carried out to update u^* and v^* from (10) using the updated boundary conditions.
(f) A new estimate for ϕ^{n+1} is generated by one ADI sweep on the discretized Poisson equation (7) with boundary conditions (16).
(g) The process is repeated to convergence.

The iterations are terminated when the maximum relative difference between the values of velocities and pressure in two successive iterations is smaller than 10^{-6} and the maximum discretized $h|\nabla_h \cdot \mathbf{u}^{n+1}|$, falls below 10^{-9} times the sum of the moduli of the velocity components. These values were chosen on the basis of standard convergence studies which showed that relaxing these limits did not appreciably change the results.

The grid generation process is also iterative as described in [38].

The values of the Courant number quoted below are found from

$$Co = \frac{U_{\text{ref}} \Delta t}{\min(h_\xi \Delta \xi, h_\eta \Delta \eta)}, \tag{46}$$

where U_{ref} is a characteristic velocity and the minimum is calculated over the entire initial grid. This procedure was followed in order to maintain a constant time step, which is required to examine the convergence rate. In general applications of the method, it might be more appropriate to use a variable time step, with the Courant number defined in a similar way, but in terms of the instantaneous values of velocities and mesh sizes.

7. Application to some free-surface problems

We now illustrate how the method performs on some actual free-surface flow problems. The first example deals with a spherical bubble and is studied for the purpose of validating the method by comparison with the semi-analytical results available for this case. Next we study both linear and non-linear shape oscillations of a bubble. We conclude with the simulation of the buoyant rise of a bubble in an unbounded fluid and compare with earlier solutions.

Implementation of the method requires that the distortion function be prescribed. On the basis of the analysis of [38], we used two main types

$$f_n = M \frac{a}{b - \eta^n}, \quad n = 1, 2, \tag{47}$$

where M is the conformal modulus, b an arbitrary constant, and a determined from the value assigned to b so as to meet the constraint given in [38].

7.1. Radial gas bubble oscillations

The spherical dynamics of a gas bubble of radius $R(t)$ in an unbounded liquid is governed by the Rayleigh–Plesset equation

$$R\frac{d^2R}{dt^2} + \frac{3}{2}\left(\frac{dR}{dt}\right)^2 = \frac{1}{\rho}\left[p_g - P_\infty - \frac{2\sigma}{R} - \frac{4\mu}{R}\frac{dR}{dt}\right], \tag{48}$$

where p_g is the bubble internal pressure, which we calculate from the isothermal relation

$$p_g = \frac{V_0}{V}p_{g0}, \tag{49}$$

in which $V = (4/3)\pi R^3$, with p_{g0} and V_0 are initial values, and P_∞ is the (constant) ambient pressure. In order to provide a more faithful test of the numerical method, we have modified this equation to reflect the fact that, in the computation, the pressure boundary condition is imposed at a distance S from the bubble center rather than at infinity. This modified equation is readily derived and is

$$\frac{S-R}{S}\left\{R\frac{d^2R}{dt^2} + \left[2 - \frac{(S^2+R^2)(S+R)}{2S^3}\right]\left(\frac{dR}{dt}\right)^2\right\} = \frac{1}{\rho}\left[p_g - P_S - \frac{2\sigma}{R} - \frac{4\mu}{R}\frac{dR}{dt}\right]. \tag{50}$$

The liquid velocity and pressure fields are given by

$$u(r) = \frac{R^2}{r^2}\frac{dR}{dt}, \tag{51}$$

$$p(r) = P_S + \frac{R(S-r)}{r(S-R)}\left(p_g - P_S - \frac{2\sigma}{R} - \frac{4\mu}{R}\frac{dR}{dt}\right) + \frac{1}{2}\rho\left(\frac{dR}{dt}\right)^2\left[\frac{R(S-r)(S^2+R^2)(S+R)}{rS^4} - \frac{R^4}{r^4} + \frac{R^4}{S^4}\right]. \tag{52}$$

In the solution for ϕ, a constant pressure is specified on the outer boundary $r = S$. For the tangential velocity u_ξ, we specify a vanishing normal derivative, while for the normal velocity u_η we impose the incompressibility condition $\nabla \cdot \mathbf{u} = 0$. For the tangential and normal components of $\mathbf{u}^*$, we use (13) and $\nabla \cdot \mathbf{u}^* = 0$, the latter implemented as in (45). The form f_2 with $b = 8$ was used for the distortion function.

Fig. 3 shows a comparison between the solution of (50) and our numerical results with the pressure-increment method for the first two cycles of oscillation of a bubble with an initial radius of 1 mm. The two results are virtually indistinguishable. The initial internal pressure is 100 kPa, the ambient pressure 200 kPa, and the liquid water with $\rho = 10^3$ kg/m^3, $\sigma = 0.0729$ J/m^2, $\mu = 0.001138$ kg/(m s). The radius S of the outer boundary was taken as 20 times the bubble initial radius, the time step was 0.5 μs, and a 40×40 grid was used. The reference velocity was the characteristic bubble wall velocity $U_{ref} = [(2/3)(P_\infty - p_{g0})/\rho]^{1/2} \simeq 8.16$ m/s. The Courant number calculated according to (46) was 0.17.

A more quantitative picture of the performance of the two projection methods can be gained from Tables 5 and 6, which show the L_1 and L_∞ norms of the error for the pressure and radial velocity v as computed by the two methods with different grid resolution; the azimuthal velocity u vanishes identically for this problem and is not shown. The last column shows the estimated convergence rate, at $t = 30$ μs; the Courant number was kept fixed at 0.26. Here, for the velocity components, the errors have been normalized by dividing by the characteristic bubble wall velocity U_{ref} while, for the pressure, the results shown have been normalized with the characteristic pressure difference $P_S - p_{g0} = 100$ kPa. For both methods, the convergence rate of the L_1 norm for the pressure and the radial velocity is close to 2. The L_∞ norm exhibits a somewhat slower convergence rate, as often found.

For the convergence test, we have used the distortion function f_1 defined in (47) with $b = 1.01$, which produces a denser grid near the bubble surface which gradually becomes less dense away from it. Use of the form f_2 with different values of b between 1.005 and 8 gave results with a comparable accuracy. However, while the rate of decrease of the L_1 error was similar to that shown in the tables, that of the L_∞ error was as low as 1.4. This second form of the distortion function results in a faster growth with distance from the free surface of the node spacing in the radial direction, which probably explains the somewhat inferior result (see e.g. [63]).
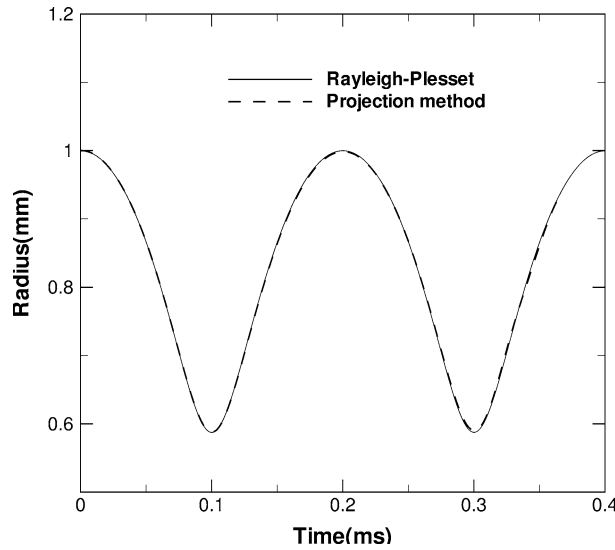
Fig. 3. Comparison between the Rayleigh–Plesset solution (solid line) and the present results (dashed) as computed with the pressure-increment method.

Table 5
Normalized L_1- and L_∞-errors in the pressure and velocity for the Rayleigh–Plesset test of Section 7.1 with the pressure-free method; the Courant number is 0.26

	20×20	30×30	40×40	Rate
Pressure				
L_1	1.73e − 3	7.51e − 4	3.68e − 4	2.22
L_∞	4.94e − 3	2.27e − 3	1.16e − 3	2.08
v-Component of velocity				
L_1	3.00e − 3	1.15e − 3	6.68e − 4	2.18
L_∞	9.37e − 3	4.17e − 3	2.67e − 3	1.82

For this problem, the exact *u* velocity component vanishes identically and is not shown.

7.2. Bubble shape oscillations

Due to surface tension, a bubble released with an initial prolate shape will execute damped oscillations. The linear theory for this process is well developed (see e.g. [64,65]) and a weakly non-linear theory was developed in [66,67]. To test our method, we consider a gas bubble in water initialized with the shape

$$r(\theta) = R[1 + \epsilon P_2(\cos \theta)], \tag{53}$$

with P_2 the second Legendre polynomial; the internal pressure was calculated using (49) as before. To compare with the exact linear theory result we took $R = 0.5$ mm and $\epsilon = 0.04$ with the same physical properties used before. With these numerical values, the difference between initial and asymptotic regimes [65,9] is negligible. The theoretical results for the oscillation period and damping rate are 2.375 and 10.98 ms. The numerical result with a 40×40 grid depended slightly on the size of the computational domain. With an outer boundary placed at a distance of $20R$, the period was found to be 2.32 ms and the damping rate 10.2 ms; with a domain size $120R$, the corresponding results were 2.36 and 10.9 ms, respectively. On the outer boundary, we imposed the same conditions as in the previous test case.

We carried out another test in the non-linear regime taking $\epsilon = 0.25$ and $R = 1$ mm. With a domain size of $20R$, the first three computed periods were 6.90, 7.08, and 7.15 ms to be compared with the result of [66] (as corrected in [67]) 7.05 ms; no theoretical results are available for the damping rate in this regime.

Table 6
Normalized L_1- and L_∞-errors in the pressure and velocity for the Rayleigh–Plesset test of Section 7.1 with the pressure-increment method; the Courant number is 0.26

	20×20	30×30	40×40	Rate
Pressure				
L_1	1.22e − 3	5.25e − 4	3.47e − 4	1.83
L_∞	3.61e − 3	1.75e − 3	1.20e − 4	1.60
v-Component of velocity				
L_1	3.69e − 3	1.45e − 3	8.41e − 4	2.14
L_∞	1.15e − 2	5.09e − 3	3.21e − 3	1.85

For this problem, the exact *u* velocity component vanishes identically and is not shown.

For a study of the convergence rate, we take $\epsilon = 0.25$ and $R = 0.5$ mm, with a domain of size 40 R. The characteristic velocity is $\sqrt{3\sigma/\rho R} \simeq 661$ mm/s and the characteristic pressure $3\sigma/R \simeq 0.437$ kPa (the maximum curvature is about $3/R$). We fixed the Courant number at 0.34 and used grids of 20×20, 30×30, 40×40; a fine 120×120 grid was assumed to give an essentially exact result. Table 7, where the errors were evaluated at $t = 0.48$ ms (about 1/4 period), shows a convergence close to quadratic for pressure and velocity for the pressure-increment method. The corresponding results for the pressure-free method are quite close and are not shown for brevity.

A test of the effect of Δt was carried out according to the method described at the end of Section 4 with a 40×40 grid. The time steps used were $\Delta t = 0.8$, 0.6, and 0.4 µs; $\Delta t = 0.6$ µs is the same time step as used for the results of Table 7 with a 40×40 grid. Results for the pressure-free method are shown in Table 8 (at the same time as for Table 7), and confirm the second-order accuracy in time of the method. The corresponding results for the pressure-increment method are basically identical and are not shown.

For these calculations, we used the distortion function f_1 with $b = 1.01$.

7.3. Buoyant rise of a gas bubble

We now illustrate the accuracy of our code by simulating the buoyant rise of a gas bubble in an infinite liquid expanse and comparing with published results. The bubble is released as a sphere with zero velocity and deforms as the motion develops.

The bubble surface corresponds to $\eta = 1$ and the external boundary, $\eta = 0$, is taken as a sphere with a radius of 20 times the equivalent bubble radius. Tests done with an outer radius 50% greater or smaller revealed negligible differences. The center of the sphere is taken at the midpoint between the points of intersection of the bubble surface with the axis of symmetry and is therefore displaced at each time step. On the

Table 7
Normalized L_1- and L_∞-errors in the pressure and the velocity for the shape oscillation test of Section 7.2 with the pressure-increment method

	20×20	30×30	40×40	Rate
Pressure				
L_1	8.82e − 3	3.26e − 3	1.51e − 3	2.54
L_∞	3.34e − 2	1.46e − 2	7.01e − 3	2.23
u-Component of velocity				
L_1	5.62e − 3	2.47e − 3	1.47e − 3	1.94
L_∞	5.56e − 2	2.61e − 2	1.60e − 2	1.80
v-Component of velocity				
L_1	7.88e − 3	3.59e − 3	2.20e − 3	1.85
L_∞	6.13e − 2	2.88e − 2	1.85e − 2	1.74

The Courant number is 0.34 and the results are evaluated at $t = 0.48$ ms, i.e. slightly before 1/4 of the first oscillation. The errors are computed with respect to a reference solution obtained with a 120×120 grid.

Table 8
Normalized L_1- and L_∞-errors in the pressure and the velocity for the shape oscillation test of Section 7.2 with the pressure-increment method for different time steps on a 40×40 grid

	Δt_1	Δt_2	Δt_3	Rate
Pressure				
L_1	4.40e − 4	2.38e − 4	9.89e − 5	2.15
L_∞	1.38e − 2	7.90e − 3	3.56e − 3	1.96
u-Component of velocity				
L_1	4.17e − 4	2.12e − 4	7.98e − 5	2.39
L_∞	1.34e − 2	7.30e − 3	3.05e − 3	2.14
v-Component of velocity				
L_1	6.04e − 4	3.09e − 4	1.17e − 5	2.38
L_∞	9.03e − 3	4.88e − 3	2.03e − 3	2.15

The Courant numbers were 0.45, 0.34, 0.23; the results are evaluated at $t = 0.48$ ms, i.e. slightly before 1/4 of the first oscillation. The errors are computed with respect to a reference solution obtained with $\Delta t = 0.1 \, \Delta t_3 = 0.04$ μs.

Table 9
The first group of columns shows results from [37] for the dependence of the drag coefficient C_D on the Reynolds and Weber numbers for a bubble rising under buoyancy

Reference results			Present results		
Re	We	C_D	Re	We	C_D
10	2	2.92	10	2	3.00
10	12	4.25	10	12	4.30
20	2	1.74	20	2	1.77
20	8	2.97	20	8	3.00
100	2	0.54	100	2	0.53
100	4	0.81	100	4	0.83
200	2	0.33	203	2	0.32

The second group of columns shows the corresponding results obtained in the present simulations.

outer boundary we impose the same conditions as for the previous test case, except that gravity is included in the specified pressure field. A 40×40 grid was used as in the previous examples with the distortion function f_2 with $b = 8$.

Published steady-state results for the drag coefficient $C_D = 4gD/3U^2$ [37,39] are given in terms of the Reynolds $Re = DU/v$ and Weber $We = \rho D U^2/\sigma$ numbers. Here D is the equivalent spherical diameter and U is the terminal velocity. For this comparison, we prescribe the radius and the physical properties of the liquid on the basis of these results and calculate the terminal velocity. If our calculation is correct, the values of Re, We, and C_D as obtained with our terminal velocity should match those used to establish the initial conditions.

A comparison with some results of [37] are shown in Table 9; the results are shown to the same accuracy as those given in that paper. The differences are at most of the order of 2–3%. It should be noted that none of the convergence difficulties caused by the free-surface boundary conditions reported earlier [37,68,69] were encountered in our calculation. An attempt to carry out the same calculation for $Re = 200$ and $We = 10$, however, failed as a region of very high curvature at the edge of the hemispherical cap gradually develops. This failure can be imputed to the grid generation part of the algorithm. We have found that, with an increase in the number of nodes, failure is delayed but we have not tried to complete the calculation due to reasons of time.

It may be noted that, in order to prevent spurious volume oscillations which, with their high frequency, force the use of an undesirably small time step, it is necessary to calculate the bubble volume accurately. We used a cubic spline approximation of the bubble surface for this purpose.

8. Summary and conclusions

This paper has described a second-order projection method for the solution of the Navier–Stokes equations in the presence of a free surface. This feature, and the associated boundary conditions, prevent a direct appli-

cation of earlier approaches and a suitable adaptation of the method has been necessary. In addition to this adaptation, a strong motivation of this work was to develop a high-accuracy method which could be used to validate free-surface three-dimensional codes under development in our group and elsewhere. In particular, we were interested in formulating a method capable of resolving thin boundary layers near the interface for future use in the calculation of processes involving phase-change, mass diffusion, and others. For this reason we have adopted boundary-fitted coordinates which have been successfully integrated with the projection method.

Comparison of our code with available theoretical predictions for volume and shape oscillations of a gas bubble and with earlier computational results for the buoyant rise of bubbles in liquids has proven its accuracy and reliability. In particular, instability problems encountered by previous investigators were found to be absent in the present approach.

Acknowledgments

References

[1] A. Esmaeeli, G. Tryggvason, Direct numerical simulation of bubbly flows. Part I. Low Reynolds number arrays, J. Fluid Mech. 377 (1998) 313–345.

[2] D.J. Torres, J.U. Brackbill, The point-set method: front-tracking without connectivity, J. Comput. Phys. 165 (2000) 620–644.

[3] G. Tryggvason, B. Bunner, A. Esmaeeli, D. Juric, N. Al-Rawahi, W. Tauber, J. Han, S. Nas, Y. Jan, A front-tracking method for computations of multiphase flow, J. Comput. Phys. 169 (2001) 708–759.

[4] G. Tryggvason, B. Bunner, A. Esmaeeli, D. Juric, N. Al-Rawahi, Computations of multiphase flows, Adv. Appl. Mech. 39 (2003) 81–120.

[5] C. Song, A.I. Sirviente, A numerical study of breaking waves, Phys. Fluids 16 (2004) 2649–2667.

[6] Y. Hao, A. Prosperetti, A numerical method for three-dimensional gas–liquid flow computations, J. Comput. Phys. 196 (2004) 126–144.

[7] F.S. de Sousa, N. Mangiavacchi, L.G. Nonato, A. Castello, M.F. Tome, V.G. Ferreira, J.A. Cuminato, S. McKee, A front tracking/front capturing method for the simulation of 3D multi-fluid flows with free surfaces, J. Comput. Phys. 198 (2004) 469–499.

[8] E. Aulisa, S. Manservisi, R. Scardovelli, A surface marker algorithm coupled to an area-preserving marker redistribution method for three-dimensional interface tracking, J. Comput. Phys. 197 (2004) 555–584.

[9] S. Popinet, S. Zaleski, Bubble collapse near a solid boundary: a numerical study of the influence of viscosity, J. Fluid Mech. 464 (2002) 137–163.

[10] A. Esmaeeli, G. Tryggvason, Computation of film boiling. Part I: numerical method, Int. J. Heat Mass transfer 47 (2004) 5451–5461.

[11] R. Scardovelli, S. Zaleski, Direct numerical simulation of free-surface and interfacial flow, Annu. Rev. Fluid Dyn. 31 (1999) 567–603.

[12] Y. Renardy, M. Renardy, PROST: A parabolic reconstruction of surface tension for the volume-of-fluid method, J. Comput. Phys. 183 (2002) 400–421.

[13] R. Scardovelli, S. Zaleski, Interface reconstruction with least-square fit and split Eulerian–Lagrangian advection, Int. J. Numer. Meth. Fluids 41 (2003) 251–274.

[14] J.E. Pilliod, E.G. Puckett, Second-order accurate volume-of-fluid algorithms for tracking material interfaces, J. Comput. Phys. 199 (2004) 465–502.

[15] J. López, J. Hernández, P. Gómez, F. Faura, A volume of fluid method based on multidimensional advection and spline interface reconnection, J. Comput. Phys. 195 (2004) 718–742.

[16] K.M.T. Kleefsman, G. Fekken, A.E.P. Veldman, B. Iwanowski, B. Buchner, A volume-of-fluid based simulation method for wave impact problems, J. Comput. Phys. 206 (2005) 363–393.

[17] S. Osher, R. Fedkiw, Level set methods: an overview and some recent results, J. Comput. Phys. 169 (2001) 463–502.

[18] D. Enright, R. Fedkiw, J. Ferziger, I. Mitchell, A hybrid particle level set method for improved interface capturing, J. Comput. Phys. 183 (2002) 83–116.

[19] J. Sethian, P. Smereka, Level set methods for fluid interfaces, Annu. Rev. Fluid Mech. 35 (2003) 341–372.

[20] H. Takahira, T. Horiuchi, S. Banerjee, An improved three-dimensional level set method for gas–liquid two-phase flows, J. Fluids Eng. 126 (2004) 578–585.

[21] A. Mukherjee, V.K. Dhir, Study of lateral merger of vapor bubbles during nucleate pool boiling, J. Heat Transfer 126 (2004) 1023–1039.

[22] S.P. van der Pijl, A. Segal, C. Vuik, P. Wesseling, A mass-conservation level-set method for modelling of multi-phase flows, Int. J. Numer. Meth. Fluids 47 (2005) 339–361.

[23] H.D. Ceniceros, A.M. Roma, A multi-phase flow method with a fast geometry-based fluid indicator, J. Comput. Phys. 205 (2005) 391–400.

[24] R. Caiden, R. Fedkiw, C. Anderson, A numerical method for two-phase flow consisting of separate compressible and incompressible regions, J. Comput. Phys. 166 (2001) 1–27.

[25] R. Fedkiw, Coupling an Eulerian fluid calculation to a Lagrangian solid calculation with the ghost fluid method, J. Comput. Phys. 175 (2002) 200–224.

[26] T.G. Liu, B.C. Khoo, C.W. Wang, The ghost fluid method for compressible gas–water simulation, J. Comput. Phys. 204 (2005) 193–221.

[27] Z.L. Li, M.C. Lai, Immersed interface method for the Navier–Stokes equations with singular forces, J. Comput. Phys. 171 (2001) 822–842.

[28] M. Francois, W. Shyy, Computations of drop dynamics with the immersed boundary method, Part 1: Numerical algorithm and buoyancy-induced effect, Numer. Heat Tr. B-Fund. 44 (2003) 101–118.

[29] R. Mittal, G. Iaccarino, Immersed boundary methods, Annu. Rev. Fluid Mech. 37 (2005) 239–261.

[30] T. Ye, W. Shyy, J. Chung, A fixed-grid, sharp-interface method for bubble dynamics and phase change, J. Comput. Phys. 174 (2001) 781–815.

[31] H.S. Udaykumar, R. Mittal, P. Rampunggoon, A. Khanna, A sharp interface Cartesian grid method for simulating flows with complex moving boundaries, J. Comput. Phys. 174 (2001) 345–380.

[32] S. Marella, S. Krishnan, H. Liu, H.S. Udaykumar, Sharp interface Cartesian grid method I: an easily implemented technique for 3D moving boundary computations, J. Comput. Phys. 210 (2005) 1–31.

[33] Y. Yang, H.S. Udaykumar, Sharp interface Cartesian grid method II: solidification of pure materials and binary solutions, J. Comput. Phys. 210 (2005) 55–74.

[34] P.E. Raad, R. Bidoae, The three-dimensional Eulerian–Lagrangian marker and micro cell method for the simulation of free surface flows, J. Comput. Phys. 203 (2005) 668–699.

[35] E. Shirani, N. Ashgriz, J. Mostaghimi, Interface pressure calculation based on conservation of momentum for front capturing methods, J. Comput. Phys. 203 (2005) 154–175.

[36] G. Ryskin, L. Leal, Orthogonal mapping in two dimensions, J. Comput. Phys. 98 (1983) 254–268.

[37] G. Ryskin, L. Leal, Numerical solution of free-boundary problems in fluid mechanics. Part I. The finite-difference technique, J. Fluid Mech. 148 (1984) 1–17.

[38] R. Duraiswami, A. Prosperetti, Orthogonal mapping in two dimensions, J. Comput. Phys. 98 (1992) 254–268.

[39] S. Takagi, A. Prosperetti, Y. Matsumoto, Drag coefficient of a gas bubble in an axisymmetric shear flow, Phys. Fluids 6 (1994) 3186–3188.

[40] S. Takagi, Y. Matsumoto, H. Huang, Numerical analysis of a single rising bubble using boundary-fitted coordinate system, JSME Int. J. B40 (1997) 42–50.

[41] D. Brown, R. Cortez, M. Minion, Accurate projection methods for the incompressible Navier–Stokes equations, J. Comput. Phys. 168 (2001) 464–499.

[42] J. Kim, P. Moin, Application of fractional-step method to incompressible Navier–Stokes equations, J. Comput. Phys. 59 (1985) 308–323.

[43] J. Bell, P. Colella, H. Glaz, A second-order projection method for the incompressible Navier–Stokes equations, J. Comput. Phys. 85 (1989) 257–283.

[44] G.E. Karniadakis, M. Israeli, S.A. Orszag, High-order splitting methods for the incompressible Navier–Stokes equations, J. Comput. Phys. 97 (1991) 414–443.

[45] Y. Zang, R.L. Street, J.R. Koseff, A non-staggered grid, fractional step method for time-dependent incompressible Navier–Stokes equations in curvilinear coordinates, J. Comput. Phys. 114 (1994) 18–33.

[46] M. Liu, Y.-X. Ren, H. Zhang, A class of fully second-order accurate projection methods for solving the incompressible Navier–Stokes equations, J. Comput. Phys. 200 (2004) 325–346.

[47] M.L. Minion, Semi-implicit projection methods for incompressible flow based on spectral deferred corrections, Appl. Numer. Math. 48 (2004) 369–387.

[48] H. Johnston, J.-G. Liu, Accurate, stable, and efficient Navier–Stokes solvers based on explicit treatment of the pressure term, J. Comput. Phys. 199 (2004) 221–259.

[49] S. Abide, S. Viazzo, A 2D compact fourth-order projection decomposition method, J. Comput. Phys. 206 (2005) 252–276.

[50] M. Sussman, A second-order coupled level set and volume-of-fluid method for computing growth and collapse of vapor bubbles, J. Comput. Phys. 187 (2003) 110–136.

[51] T. Chen, P.D. Minev, K. Nandakumar, A projection scheme for incompressible multiphase flow using adaptive Eulerian grid, Int. J. Numer. Meth. Fluids 45 (2004) 1–19.

[52] D. Lörstad, L. Fuchs, High-order surface tension VOF-model for 3D bubble flows with high density ratio, J. Comput. Phys. 200 (2004) 153–176.

[53] J. Brackbill, D. Kothe, C. Zemach, A continuum method for modeling surface tension, J. Comput. Phys. 100 (1992) 335–354.

[54] P.M. Gresho, R.L. Sani, On pressure boundary conditions for the incompressible Navier–Stokes equations, Int. J. Numer. Meth. Fluids 7 (1987) 1111–1145.

[55] P.M. Gresho, Incompressible fluid dynamics: some fundamental formulation issues, Annu. Rev. Fluid Mech. 23 (1991) 413–453.

[56] F. Mashayek, N. Ashgriz, A hybrid finite-element–volume-of-fluid method for simulating free surface flows and interfaces, Int. J. Numer. Meth. Fluids 20 (1995) 1363–1380.

[57] S. Chen, D. Johnson, P. Raad, Velocity boundary conditions for the simulation of free surface fluid flow, J. Comput. Phys. 116 (1995) 262–276.

[58] D. Juric, G. Tryggvason, Computation of boiling flows, Int J. Multiphase Flow 24 (1998) 387–410.

[59] G. Son, V. Dhir, Numerical simulation of film boiling near critical pressures with a level set method, J. Heat Transfer 120 (1998) 183–192.
[60] S. Orszag, M. Israeli, M. Deville, Boundary conditions for incompressible flows, J. Scient. Comput. 1 (1986) 75–111.
[61] E. Weiann, J.G. Liu, Projection method. I. Convergence and numerical boundary layers, SIAM J. Numer. Anal. 32 (1995) 1017–1057.
[62] J. Thompson, B. Soni, N. Weatherill, Handbook of Grid Generation, CRC Press, Boca Raton, 1999.
[63] L. Gamet, F. Ducros, F. Nicoud, T. Poinsot, Compact finite difference schemes on non-uniform meshes. Application to direct numerical simulations of compressible flows, Int. J. Numer. Meth. Fluids 29 (1999) 159–191.
[64] A. Prosperetti, Normal-mode analysis for the oscillations of a viscous liquid drop in an immiscible liquid, J. Mécanique 19 (1980) 149–182.
[65] A. Prosperetti, Free oscillations of drops and bubbles: The initial-value problem, J. Fluid Mech. 100 (1980) 333–347.
[66] J. Tsamopoulos, R. Brown, Nonlinear oscillations of inviscid drops and bubbles, J. Fluid Mech. 127 (1983) 519–537 (correction in next paper).
[67] J. Tsamopoulos, R. Brown, Resonant oscillations of inviscid charged drops, J. Fluid Mech. 147 (1983) 373–395.
[68] W.J. Silliman, L.E. Scriven, Separating flow near a static contact line: slip at a wall and shape of a free surface, J. Comput. Phys. 34 (1980) 287–313.
[69] H. Saito, L.E. Scriven, Study of coating flow by the finite element method, J. Comput. Phys. 42 (1981) 53–76.